Ultramicroscopy 148 (2015) 57–66

Contents lists available at ScienceDirect

Ultramicroscopy

journal homepage: www.elsevier.com/locate/ultramic

# Effects of laser energy and wavelength on the analysis of $LiFePO_4$ using laser assisted atom probe tomography

Dhamodaran Santhanagopalan [a,1], Daniel K. Schreiber [b,1], Daniel E. Perea [c], Richard L. Martens [d], Yuri Janssen [e], Peter Khalifah [e,f], Ying Shirley Meng [a,*]

[a] Department of NanoEngineering, University of California San Diego, CA 92093, USA
[b] Energy and Environment Directorate, Pacific Northwest National Laboratory, Richland, WA 99354, USA
[c] Environmental Molecular Sciences Laboratory, Pacific Northwest National Laboratory, Richland, WA 99354, USA
[d] Central Analytical Facility, University of Alabama, Tuscaloosa, AL 35487, USA
[e] Department of Chemistry, Stony Brook University, Stony Brook, NY 11790-3400, USA
[f] Department of Chemistry, Brookhaven National Laboratory, Upton, NY 11793-5000, USA

ARTICLE INFO

*Article history:*
Received 24 March 2014
Received in revised form
5 September 2014
Accepted 8 September 2014
Available online 21 September 2014

*Keywords:*
Atom probe tomography
$LiFePO_4$
Oxides
Stoichiometry
Molecular dissociation

ABSTRACT

The effects of laser wavelength (355 nm and 532 nm) and laser pulse energy on the quantitative analysis of $LiFePO_4$ by atom probe tomography are considered. A systematic investigation of ultraviolet (UV, 355 nm) and green (532 nm) laser assisted field evaporation has revealed distinctly different behaviors. With the use of a UV laser, the major issue was identified as the preferential loss of oxygen (up to 10 at%) while other elements (Li, Fe and P) were observed to be close to nominal ratios. Lowering the laser energy per pulse to 1 pJ/pulse from 50 pJ/pulse increased the observed oxygen concentration to nearer its correct stoichiometry, which was also well correlated with systematically higher concentrations of $^{16}O_2^+$ ions. Green laser assisted field evaporation led to the selective loss of Li (~33% deficiency) and a relatively minor O deficiency. The loss of Li is likely a result of selective dc evaporation of Li between or after laser pulses. Comparison of the UV and green laser data suggests that the green wavelength energy was absorbed less efficiently than the UV wavelength because of differences in absorption at 355 and 532 nm for $LiFePO_4$. Plotting of multihit events on Saxey plots also revealed a strong neutral $O_2$ loss from molecular dissociation, but quantification of this loss was insufficient to account for the observed oxygen deficiency.

Published by Elsevier B.V.

## 1. Introduction

Li-ion batteries play a major role in energy storage devices, and high energy density battery cathode materials, such as $LiFePO_4$ (LFP), are critical to achieve improved safety and performance. The mechanism of lithium intercalation in LFP at different length scales has been an intense area of research [1–4]. The phase boundary chemistry and three-dimensional morphology of the LFP/FP interface have yet to be visualized and understood with high spatial resolution. Such visualization is necessary to understand the intercalation mechanism of LFP and improve its performance. Atom probe tomography (APT) has matured as a useful technique for three-dimensional analysis of compositional variations with sub-nanometer spatial resolution for a wide-range of materials systems [5–10]. APT relies on field ionization of atoms from the apex of a needle-shaped specimen, the physics of which is relatively well understood for metals using a voltage-pulsed method. By comparison, thermally-assisted field evaporation of insulating materials (e.g. oxide ceramics) with ultra-fast lasers is a much more recent development [11–14], and a good understanding of the underlying physics and experimental uncertainty associated with these measurements remains to be achieved. APT measurements of bulk oxide materials have often found oxygen stoichiometries that are deficient relative to expected values [14–19], and the origins of these non-stoichiometric measurements are uncertain and still debated. These studies do, however, demonstrate the importance of further systematic studies to identify and understand stoichiometric errors that may accompany laser-assisted APT examinations, especially for complex oxide materials.

In this paper, we present systematic studies of the effects of laser wavelength and pulse energy on the APT analysis of complex oxide systems that are relevant to Li-based battery materials systems. For $LiFePO_4$, the primary challenges are the strong P–O bonds (high probability of complex P–O molecular complexes in the mass spectra),

* Corresponding author. Tel.: +1 858-822-4247; fax: +1 858-534-9553.
*E-mail address:* shirleymeng@ucsd.edu (Y.S. Meng).
[1] Contributed equally for the work.

http://dx.doi.org/10.1016/j.ultramic.2014.09.004
0304-3991/Published by Elsevier B.V.

the relatively low evaporation field for Li (~14 V/nm) and issues related to general oxygen loss in bulk oxides. LFP was selected as a technologically-relevant lithium ion battery material as well. Quantification of constituent elements in LFP, particularly lithium, is critical to the understanding of phase transformations and phase boundary chemistry during delithiation/lithiation reactions within $LiFePO_4$/$FePO_4$ systems. A fundamental understanding of the phase transformation mechanism in LFP will guide the design of high energy and high power lithium ion batteries which can be safely operated. The systematic studies presented herein demonstrate the applicability and issues associated with APT of these Li-based oxide materials systems, and more broadly, provide further insights into the field evaporation phenomena of complex oxides during laser-assisted field evaporation.

## 2. Materials and methods

Needle-shaped APT specimens of LFP were fabricated by focused ion beam liftout and were mounted onto commercial silicon flat-top micro-post arrays [20]. The LFP liftouts were extracted from a single crystal grown by a flux growth method reported elsewhere [21]. All specimens were analyzed in the [100] crystal orientation, although no crystallographic features were apparent in the subsequent APT reconstructions. The tips were sharpened with a relatively low ion-beam acceleration (5 kV $Ga^+$ versus the more typical 30 kV $Ga^+$) using an annular milling pattern or a bitmap image with gradient milling pattern. The low-kV ion beam was critical to minimizing ion-beam damage in these very sensitive Li-based materials. Tips with shank angles of about 30–35° reliably produced high-quality APT data sets while smaller shank angles resulted in early fractures, particularly with green laser pulsing. The UV wavelength (355 nm) laser assisted APT data were collected at Pacific Northwest National Laboratory (LEAP 4000X HR) with a fixed specimen base temperature of 50 K, a laser repetition rate of 160 or 200 kHz and a detection rate between 0.5% and 2.5% (0.005 and 0.025 detected ions/pulse). The UV laser energy most strongly influenced the measured elemental concentration, and energy from 1 to 50 pJ/pulse was tested. The green wavelength (532 nm) laser assisted APT data were collected at University of Alabama, Tuscaloosa (LEAP 3000X Si) with specimen base temperatures of 40, 50 or 65 K, a laser repetition rate between 50 and 250 kHz and a detection rate of either 0.5% or 1%. The smallest achievable laser energy with the green laser system was limited to 200 pJ and hence the data was collected using 200 and 300 pJ/pulse energies only. Note that the LEAP 4000X HR system utilizes in-vacuum optics that enables a more focused laser spot at the specimen than the LEAP 3000X Si. To better compare results from these two different laser systems, a baseline comparison is also presented using commercially available presharpened Si microposts (Sb doped to $< 0.01\ \Omega$ cm resistivity). By comparing the Si charge state ratio as a function of laser energy, it is shown that due to combined differences in laser focus and absorption, the LEAP 3000X Si must utilize approximately 15X the laser energy readout to achieve a comparable evaporation field for Si. The 3D APT reconstructions and subsequent compositional analyses were performed using the IVAS software package (version 3.6.6) from Cameca Instruments. When possible, the final tip radius was measured by post-APT scanning electron microscopy to guide the scaling of APT reconstructions.

## 3. Results

### 3.1. Baseline comparison of the LEAP 3000X Si and the LEAP 4000X HR lasers with Si

Presharpened Si microposts were systematically analyzed as a function of laser energy with both APT systems to better understand how to compare the laser energy readouts. The premise of this comparison is that the detected ratio of charge states is a result of the field-dependent probability of post-ionization as described in detail by Kingham [22] and Haydock and Kingham [23]. Early comparative studies of the green and UV laser systems in the LEAP 3000 and 4000 tomographs on Ni-base [24] and Fe-base [25] alloys demonstrated that the larger laser spot size of the LEAP 3000 necessitates a laser energy readout ~3X that of the LEAP 4000 to achieve comparable charge state ratios in those materials. Importantly, the LEAP 4000 used in those initial studies utilized first-generation in-vacuum optics and the LEAP 4000 used in the current study has a smaller spot size still from further optimization of those optics, although exact quantification of these differences has not been published. Data were collected from Si microposts at a detection rate of 0.0055 ions/pulse on the LEAP 4000X HR and 0.008 ions/pulse on the LEAP 3000X Si to compensate for differences in the detection efficiency of the two tools (~37% and ~50%, respectively) and thus achieve a similar evaporation rate (~0.016 ions/pulse). A single Si micropost was used for each data series and data were collected in both ascending and descending laser energies to obviate any effects due to tip-radius evolution. The measured Si charge states are plotted as a function of laser energy in Fig. 1. As expected, lower laser energies correspond to higher Si charge states and thus a higher evaporation field for both the UV and green lasers. Both datasets exhibit the anticipated rapid transition from primarily $Si^{2+}$ to $Si^{1+}$ at a fairly well-defined laser energy and corresponding field strength of ~19 V/nm [22,26]. For the LEAP 3000X Si this transition occurs at a laser energy of ~900 pJ/pulse and for the LEAP 4000X HR at ~60 pJ/pulse, corresponding to an approximate factor of 15 difference. Note that this difference reflects the combined effects of the laser focus (spot size), any possible material-dependent differences in light absorption efficiency at different wavelengths, and other tool parameters (e.g. local electrode differences) that cannot be independently separated in this simple comparison. For the purposes of the discussions below we restrict the significance of this baseline comparison to state simply that for materials that efficiently absorb green and UV wavelengths of light, the differences in laser spot size necessitate a higher laser energy readout from the LEAP 3000X Si than the LEAP 4000X HR to realize a similar evaporation field.

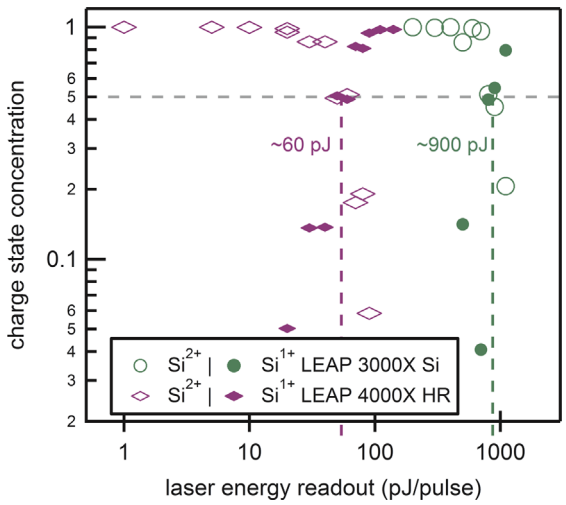


**Fig. 1.** Comparison of detected charge states from pre-sharpened Si microposts as a function of laser energy readout for the LEAP 3000X Si and the LEAP 4000X HR. The $2\sigma$ counting error is less than the symbol size for every datapoint.

### 3.2. Mass spectra analysis of $LiFePO_4$

Typical mass spectra recorded with green and UV laser assisted field evaporation are presented in Fig. 2. Numerous peaks in both spectra correspond to $PO_x$ type complex ions, which are common for phosphate containing specimens [27], while Fe and Li appear predominantly as elemental ions. Comparison of the mass spectra reveals striking differences. Numerous complex ions observed with the UV laser spectrum (e.g. $FePO_3^{2+}$, $FePO_3^{+}$, $FePO_4^{+}$ and $P_2O_5^{+}$) are not apparent in the green laser spectrum. A study on the effects of UV laser energy on ceria found a strong correlation between higher laser energies and the prevalence of large molecular species [28]. This might suggest that the increased prevalence of larger complex ions in the UV laser mass spectrum indicates a higher effective laser energy than with the green laser. It is important to note, however, that the direct effects of laser wavelength on molecular ion evaporation have not been independently explored in sufficient detail to discount its independent effects. Another major difference between the two spectra is the background level. For the green laser spectrum, the background level at small mass-to-charge-state ratios ( $<7$ Da) is substantially less than that of the UV spectrum. However, the background level above the $^{7}Li^{+}$ peak is substantially increased for the green spectrum and unchanged for the UV spectrum. This may be explained as slower tip quenching with the green laser, which results in delayed evaporation of Li from the residual elevated temperature. Slower quenching is to be expected for the green laser data as a result of a larger heated volume of material from two primary factors: the longer wavelength of the laser and thus larger interaction depth and also the larger laser spot size using the LEAP 3000 focusing optics [29].

### 3.3. Compositional analysis of $LiFePO_4$ for green and UV laser pulsing

Fig. 3(a and c) shows lateral concentration profiles extracted across the tip axis (parallel with the laser impact direction) of the entire reconstructed volume of two specimens using green and UV laser pulsing, respectively, and Fig. 3(b and d) depicts concentration depth profiles along the analysis direction for the same datasets. A prominent gradient in elemental concentrations is evident in the lateral concentration profile for the green laser dataset (Fig. 3a) that is relatively negligible in the UV laser data (Fig. 3b). The strongest of these gradients is a Li-deficiency/Fe-excess apparent at the edges of the green laser dataset. The symmetry of the concentration variations about the tip axis suggests that the laser impact direction is not a significant factor in these observations. The depth profiles depicted in Fig. 3(b and d) reveal slight composition variations near the specimen surface for both datasets. Although not plotted, the Ga concentration nearest the edges of the green laser dataset was measured to be $\sim$0.8 at% and $<0.1$ at% at the central regions while Ga concentrations for the UV laser datasets peaked at $<0.1$ at% even at the reconstruction periphery. This suggests that ion-beam damage from the FIB affected the measurements nearest the specimen surface in spite of utilizing low energy preparation conditions. This observed difference between the two datasets could result from a larger field of view for the straight-flight green laser data or inadvertent differences in sample preparation methods. Alternatively, the lateral composition variations could originate from element-specific field evaporation differences that are more pronounced under green laser evaporation conditions. Recent work by Greiwe et al. [30] has suggested that Li may redistribute within a dielectric APT specimen during analysis due field-driven ion migration, although it is not clear if this effect (observed in a thin film oxide on a metallic substrate) would also occur during the analysis of a bulk oxide. For the purposes of the analyses below, all datasets were cropped to the central $\sim$40 nm diameter to minimize these edge concentration irregularities and the first $\sim$10 nm in depth of the reconstructions were excluded from analysis. The measured Ga concentration within all of the following analyses was $<0.1$ at% and typically $<0.02$ at%.

The averaged composition measured by APT for all analysis parameters on numerous specimens (8 with green laser and 4 with UV laser) is summarized in Table 1. The experimental measurements and expected nominal values are shown in both overall at% and also as a ratio normalized to the sum of Fe+P. In general the APT measurements made with the green laser exhibit a significant Li deficiency ($\sim$4.5 at% deficiency) and a concomitant Fe excess ($\sim$4.5 at% excess), while the normalized P and O concentrations were close to the expected stoichiometric concentrations. In the UV laser data, the Li and Fe concentrations are in excess ($\sim$3 at% and $\sim$6 at% excess, respectively), O exhibits a strong deficiency ($\sim$9 at% deficiency), and there is a slight deficiency of P. Note that the nominal Li/Fe ratio of this LFP single crystal was established by inductively coupled plasma – optical emission spectroscopy (ICP-OES) analysis to be 0.95, while single crystal diffraction studies on a large number of crystals prepared under similar manner found a minimum Li/Fe ratio

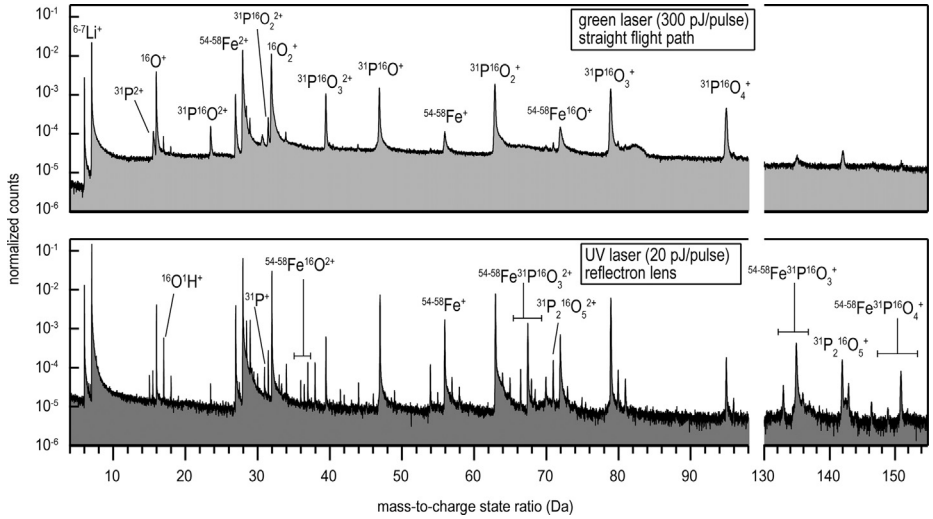


**Fig. 2.** APT mass spectra obtained using green wavelength laser pulsing (top) and UV wavelength laser pulsing (bottom). All major peaks in the top spectrum are also present in the bottom spectrum along with several additional, more complex molecular species. The vertical axis of each spectrum is normalized to the total number of counts.

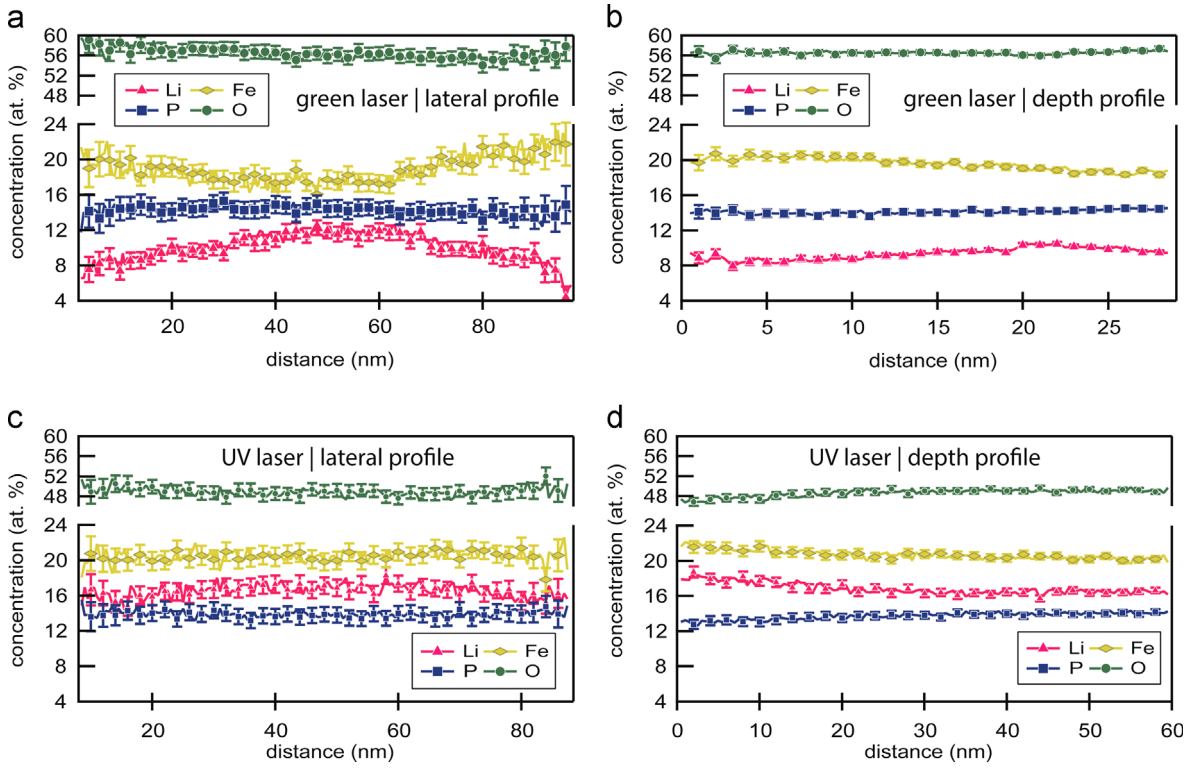


**Fig. 3.** Concentration profiles extracted (a), (c) laterally across the APT reconstructions nominally parallel with the incident laser direction and (b), (d) along the analysis direction for the green laser and the UV laser systems. Strong lateral concentration gradients are apparent for the green laser and gradients are nearly negligible for the UV laser. Error bars indicate $1\sigma$ from counting error in each plot. (For interpretation of the references to color in this figure legend, the reader is referred to the web version of this article.)

**Table 1**
Average measured atomic concentrations and ratios normalized to Fe+P for APT data acquired with either green-laser assisted field evaporation or UV-laser assisted field evaporation. The indicated error represents one standard deviation for eight specimens with the green laser and four specimens with the UV laser.

| Element | Nominal | | Green laser (8 tips) | | UV laser (4 tips) | |
|---|---|---|---|---|---|---|
| | At% | Ratio to Fe+P | At% | Ratio to Fe+P | At% | Ratio to Fe+P |
| Li | 14.3 | 0.5 | $9.7 \pm 1.9$ | $0.301 \pm 0.059$ | $17.6 \pm 0.9$ | $0.520 \pm 0.025$ |
| Fe | 14.3 | 0.5 | $18.8 \pm 0.9$ | $0.583 \pm 0.027$ | $20.5 \pm 0.4$ | $0.606 \pm 0.013$ |
| P | 14.3 | 0.5 | $13.5 \pm 0.3$ | $0.417 \pm 0.009$ | $13.3 \pm 0.2$ | $0.394 \pm 0.007$ |
| O | 57.1 | 2.0 | $57.9 \pm 1.9$ | $1.791 \pm 0.059$ | $48.4 \pm 1.2$ | $1.429 \pm 0.035$ |

of 0.97 [21]. This indicates that the apparent Li deficiency in the green laser APT data is an artifact. Since Li and O exhibit the largest differences between the UV and green laser data, a more reliable comparison of green versus UV laser datasets can be made by normalizing to the sum of the Fe+P concentrations for both sets of data. This renormalization reveals that the measured concentrations of Fe and P are similar for both laser wavelengths and that the only significant differences exist for the Li and O concentrations. In both cases, there is a slight excess of Fe and deficiency of P at similar levels. For the UV laser, the Li ratio is close to its nominal value, while for the green laser, the renormalization suggests a slight O deficiency exists despite the higher-than stoichiometric measured O concentration. This is a result of the large Li deficiency in the green laser dataset that skews upwards the measured O concentration: an artifact that was removed by renormalization to the sum of Fe+P. Note, however, that this renormalization is imperfect as it implicitly assumes that the measured concentrations of Fe and P are equally accurate for all

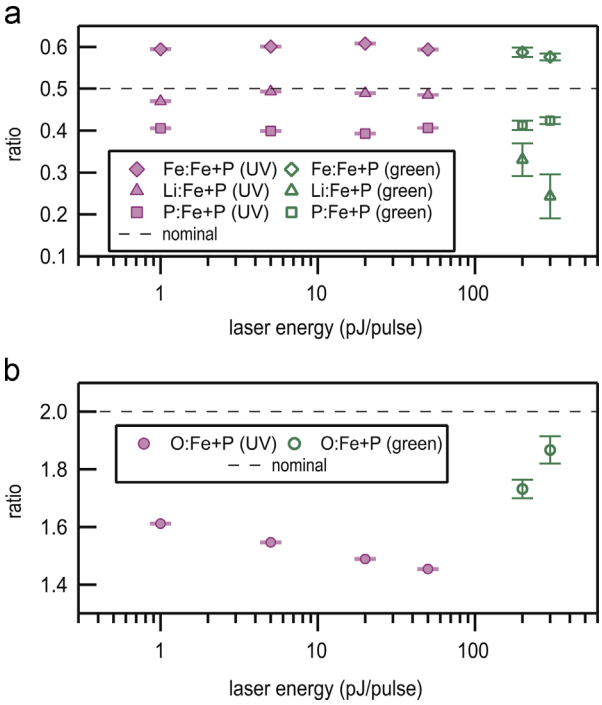


**Fig. 4.** (a and b) Elemental concentration ratios with respect to total Fe+P ions as a function of laser energy. Data from UV and green laser illumination are indicated by filled and open symbols, respectively. The UV power series was collected from a single specimen while the green laser datapoints represent averages of 3 individual specimens each (6 in total). Error bars represent $2\sigma$ from counting error for the UV laser data and one standard deviation amongst the three individual measurements for each green laser datapoint. (For interpretation of the references to color in this figure legend, the reader is referred to the web version of this article.)

experimental parameters and as such should be considered a relative improvement.

### 3.4. Effect of laser energy on the measured composition of $LiFePO_4$

Measurements of elemental concentrations (normalized to Fe+P) as a function of laser pulse energy are plotted in Fig. 4. The UV laser data series was extracted from a single tip analyzed at various energies and the indicated error is $2\sigma$ of the counting error while the green laser data represents an average of 3 specimens each for 200 and 300 pJ/pulse and the indicated error is one standard deviation amongst those measurements. The UV laser data shows a clear trend of lower O with increasing laser energy and relatively small variations in the Fe, P and Li ratios. A slight decrease in Li at the lowest laser energy (1 pJ/pulse) is also apparent, but the overall trend across all laser energies is relatively weak. Conversely, the green laser data exhibit lower Li and higher O at higher energies, although there is significant scatter as indicated by the relatively large error bars. When the green and UV laser data are compared directly, the green laser data consistently exhibit higher concentrations of O and lower concentrations of Li than the UV laser data.

The detected concentrations of major ionic species are plotted in Fig. 5 for various laser energies. The green laser data again represent the average of three specimens each for 200 pJ/pulse and 300 pJ/pulse (indicated error is the standard deviation of the three measurements) while the UV laser data are from the analysis of a single specimen and the indicated error is $2\sigma$ of the counting error from an average of 1.6 million ions per datapoint. The $^{16}O_2^+$ ion concentration at 32 Da is most strongly correlated with the UV laser energy while $PO_3^+$ and $PO_4^+$ ions also contributed to a higher oxygen concentration at lower laser energies. The measured concentration of $^{16}O_2^+$ ions increased as the laser power decreased from 50 pJ to 1 pJ from 12.5 ion% to 16.8 ion%. The apparent trends with laser energy for the green laser are not consistent with the observations of the UV laser series. Datasets with higher laser energy exhibited higher concentrations of $^{16}O_2^+$ and lower concentrations of Li, consistent with the overall composition measurements for the green laser presented in Fig. 4. Comparing the detected ionic species between the green and UV laser reveals significant differences. While the detected concentrations of Fe and the $PO_x$-type peaks are quite similar for the two lasers, the green laser data contained much higher percentages of elemental $O^+$ and $O_2^+$ species and much lower percentages of $Li^+$. The concentration of $PO_4^{n+}$ is, however, also higher for the green laser than the UV. Overall it appears that the higher concentrations of $O^+$ and $O_2^+$ species with green laser pulsing give rise to its improved oxygen stoichiometry. It is also interesting that the ratio of $O^+$:$O_2^+$ is much higher for the green laser data than the UV, which is in good agreement with similar observations of Bachhav et al. on Fe oxides at different laser wavelengths [18].

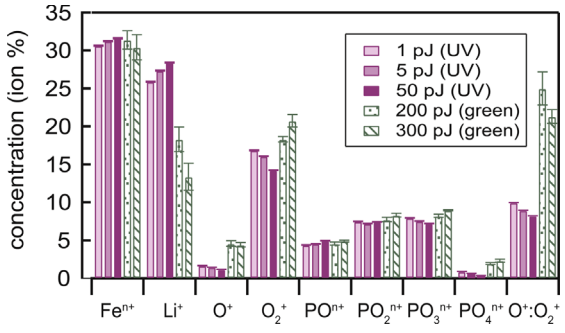


**Fig. 5.** Detected concentrations of ionic species and the ratio of $O^+$:$O_2^+$ for various laser conditions.

### 3.5. Molecular dissociation behavior and quantification

Correlation plots shown in Fig. 6 (so-called Saxey plots [31]) were constructed of multihit ion pairs to investigate other evidence for unique evaporation behavior in $LiFePO_4$. These plots were constructed from evaporation events consisting of exactly two detected ions in a single pulse (i.e. excluding events of only one ion and three or more ion pairs). This was done to maximize the signal-to-noise ratio which can be decreased by plotting higher-order evaporation events. Numerous molecular ion dissociation tracks are apparent, indicating the prominent evaporation of unstable molecules that dissociate into more stable species during post-ionization acceleration [32]. The tracks labeled 1–5 correspond to the following pathways:

(1) $^{31}P^{16}O_2^{2+} \rightarrow {}^{31}P^{16}O^+ + {}^{16}O^+$

(2a) $^{31}P^{16}O_3^{2+} \rightarrow {}^{31}P^{16}O_2^+ + {}^{16}O^+$

(2b) $^{31}P^{16}O_3^{2+} \rightarrow {}^{31}P^{16}O^+ + {}^{16}O_2^+$

(3) $^{31}P^{16}O_4^{2+} \rightarrow {}^{31}P^{16}O_2^+ + {}^{16}O_2^+$

(4) $^{31}P_2{}^{16}O_5^{2+} \rightarrow {}^{31}P^{16}O_2^+ + {}^{31}P^{16}O_3^+$

(5) $^{31}P^{16}O_4^{1+} \rightarrow {}^{31}P^{16}O_2^+ + {}^{16}O_2^0 (\infty\ \mathrm{Da})$

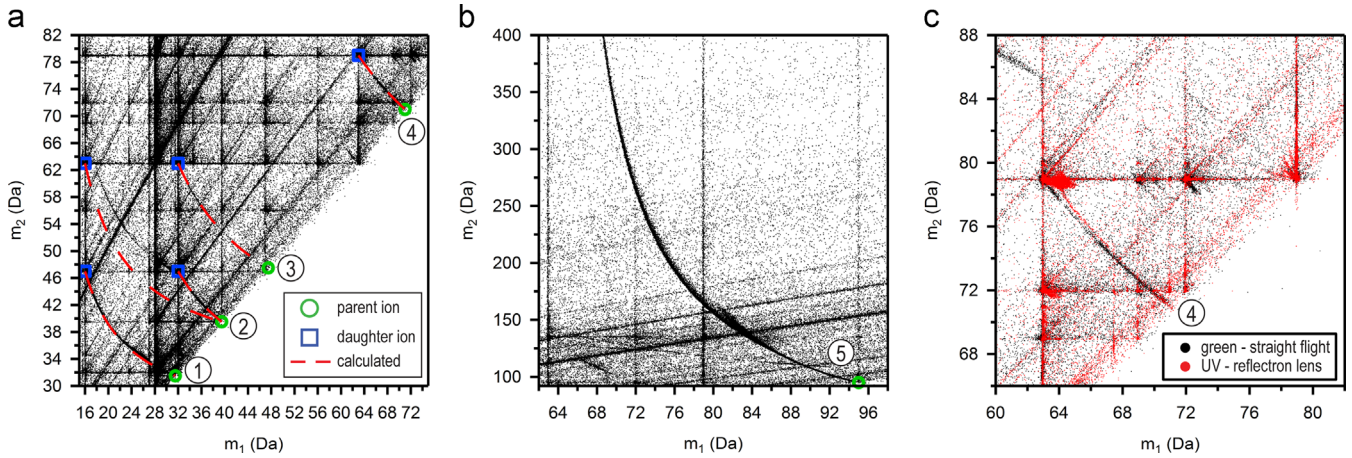


**Fig. 6.** Multihit correlation plots (Saxey plots [31]) obtained (a) and (b) with an APT equiped with a green laser and straight flight path. The molecular dissociation curves and parent/daughter ion pairs are identified within the text. (c) Higher magnification of the region around track 4 comparing the green straight flight data with that of a UV laser and reflectron lens. (For interpretation of the references to color in this figure legend, the reader is referred to the web version of this article.)

Traces for each dissociation pathway (red lines) were calculated after Saxey [31] as:

$$m_1' = m_1\left[1-\frac{\Delta V}{V_0}\left(1-\frac{m_1}{m_p}\right)\right]^{-1} \text{ and } m_2' = m_2\left[1-\frac{\Delta V}{V_0}\left(1-\frac{m_2}{m_p}\right)\right]^{-1}$$

where $m_p$, $m_1$, and $m_2$ are the mass-to-charge-state ratios of the parent molecule and two daughter molecules, respectively, and $m_1'$ and $m_2'$ are the energy deficient mass-to-charge-state ratios of the two daughter molecules. Furthermore $V_0$ is the applied voltage and $\Delta V$ is the reduction in voltage (electric field) at the point in space where the parent molecule dissociated into the two daughter molecules. Tracks 1–4 represent typical dissociation pathways commonly observed in oxide-based and III–V semiconductor systems in which a parent molecule dissociates into a pair of more stable species (e.g. $^{31}P^{16}O_2^{2+} \rightarrow {}^{31}P^{16}O^{+} + {}^{16}O^{+}$). Intriguingly, track 4 is also observed in the mulithit plot for the data obtained with a UV laser and a reflectron lens. The reflectron lens data is compared directly to the straight flight data around track 4 in Fig. 6(c). Typically the reflectron lens compensates for the energy deficits that originate from molecular dissociation near the tip apex, resulting in significantly shorter tracks that do not extend continuously from parent to daughter. Dissociation tracks that extend completely from the parent to the daughter species require a broad range of energy deficits caused by an electric field gradient. This suggests that the molecular dissociations apparent in the UV laser data occurred within the post-acceleration of the reflectron lens, far from the tip apex.

Dissociation track 5 presents a number of interesting features. This track corresponds to the prominent formation of neutral $O_2$ by the following dissociation reaction: $^{31}P^{16}O_4^{1+} \rightarrow {}^{31}P^{16}O_2^{+} + {}^{16}O_2^{0}$. Relatively weak signals for neutral molecule formation have been observed previously in similar plots for GaN materials [31], but for LFP, this dissociation pathway is the strongest observed dissociation and it indicates a propensity for the formation of an unstable $PO_4^+$ molecule that can easily dissociate. It has been conjectured that neutral O loss from the tip apex may be a key contributor to sub-stoichiometric O concentrations in APT experiments of numerous oxide systems [16,28,33], but this hypothesis is difficult to prove since APT is typically blind to the loss of neutral species from the tip. In this case, since the neutral $O_2$ molecule forms *after* accelerating towards the detector as the parent $PO_4^+$ molecule, we are able to definitively state that neutral $O_2$ formation can occur *at least* from the dissociation of complex molecules.

As noted by Saxey [31], the identification and quantification of molecular dissociation pathways provides a means to improve the quantification of APT measurements. Quantification is accomplished by first replotting the correlated ion pairs as the minimum distance of each ion pair from the calculated track trajectory versus $\Delta V/V_0$ and then counting the number of ion pairs within some specific distance of the track. This is shown schematically in Fig. 7 for track 2b: $^{31}P^{16}O_3^{2+} \rightarrow {}^{31}P^{16}O^{+} + {}^{16}O_2^{+}$. In this case ions were summed when the distance from the track was $<0.15$ Da, illustrated by a green overlay. Ions located at $\Delta V/V_0 < 0.02$ and $\Delta V/V_0 > 0.98$ were excluded from this calculation since they were primarily unrelated to the dissociation track (i.e. they originate from the co-evaporation of $PO^+$ and $O_2^+$ or two $PO_3^{2+}$ in this example). The background was

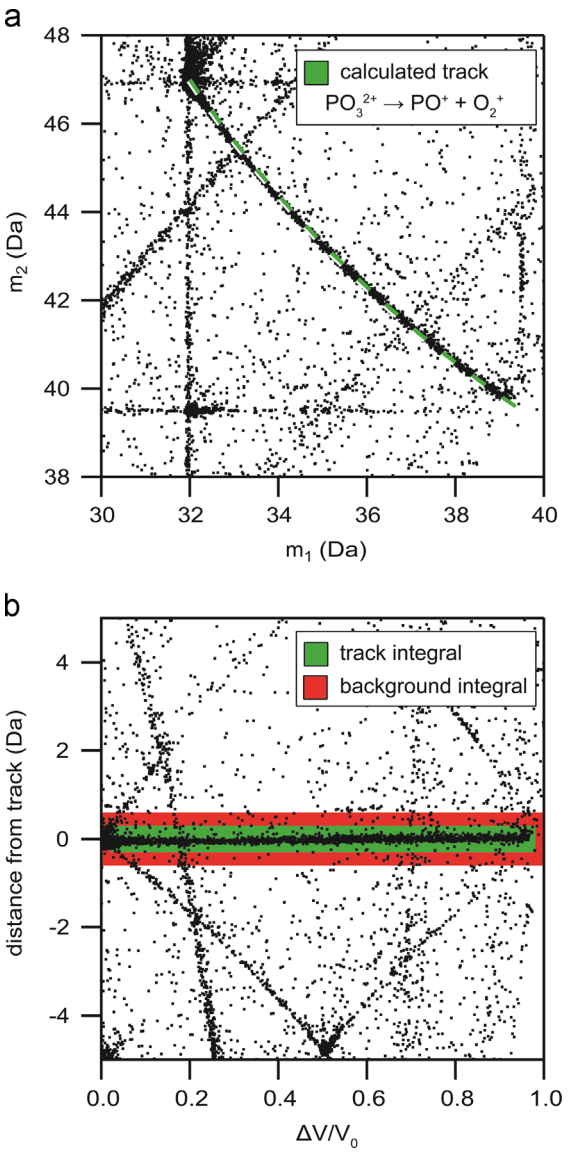


**Fig. 7.** (a) Correlation plot for track 2b and (b) the same data replotted as the distance from the analytical track versus $\Delta V/V_0$.

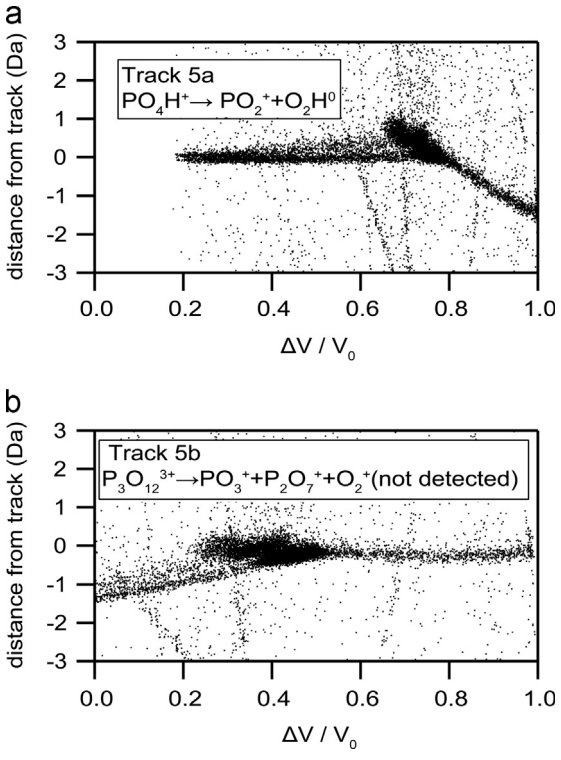


**Fig. 8.** Two possible fits to the molecular dissociation pathway about track 5: fitting to a path extending to infinity (neutral molecule formation) and (b) fitting to two finite values (174 and 79 Da).

then estimated as the number of ions with minimum distances between 0.15 and 0.3 Da, highlighted in red, to account for general background and the intersection of the dissociation track with other prominent but unrelated correlated evaporation tracks.

Closer examination of track 5 (Fig. 8) after replotting as minimum distance versus $\Delta V/V_0$ reveals unexpected features that can be used to further refine our understanding of this dissociation pathway. The minimum distance versus voltage drop is plotted about this track for the initial identification of $^{31}P^{16}O_4^{1+} \rightarrow {}^{31}P^{16}O_2^{+} + {}^{16}O_2^{0}$, with a minor modification to originate from $PO_4H^{+}$, which provided a better overall fit. From this plot it is immediately apparent that what initially appeared to be a single dissociation track is in fact composed of two distinct sections. A very good fit is obtained for the $\Delta V/V_0$ range between 0.2 (corresponding to maximum time-of-flight window for this voltage and flight path) and ~0.7 while a separate track clearly dominates the behavior outside this range. The second segment of the track is associated with a pair of finite ions (i.e. not a neutral molecule), although the exact solution for the dissociation pathway is not obvious. If the parent molecule, clearly at 95 Da, is considered to be $P_3O_{12}^{3+}$ rather than $PO_4^{+}$, a partial solution can be identified by its dissociation into three components as: $^{31}P_3{}^{16}O_{12}^{3+} \rightarrow {}^{31}P_2{}^{16}O_7^{+} + {}^{31}P^{16}O_3^{+} (+ {}^{16}O_2^{+})$. Fitting to the first two daughter ions of this pathway gives a reasonable result (Fig. 8b), but this solution neglects the final $O_2^{+}$ which should be detected as a third ion in this event. As shown in Fig. 9, when correlation plots are generated from events associated with three or more ions, this track nearly disappears while other dissociation pathways, such as track 2b, clearly persist albeit with a poorer signal to noise ratio. At this point the exact nature of this second portion of this dissociation track and the reason behind the disappearance of track 5 when imaging evaporation events with three or more ions remain unclear and possibly in conflict with the identified best fit for this region.

Quantification of the effects of the identified molecular dissociation pathways are presented in Table 2 for a representative green laser, straight flight data set collected at 200 pJ/pulse. After background subtraction, slightly less than 70,000 new ions were successfully ranged with this approach. We note that the $P_3O_{12}^{3+}$ dissociation pathway was excluded from this quantification due to the uncertainty of its identification, which is significant since it potentially accounts for approximately 50% of all the ions on dissociative pathways. Ultimately the ranged molecular dissociation events account for only 1.6% of the total ranged ions in this dataset and therefore had a very limited effect on the final oxide

**Table 2**
Measured composition for a representative green laser dataset (200 pJ/pulse) both as-ranged and after adding the counts from dissociation tracks. The indicated uncertainty represents $2\sigma$ from counting statistics.

| Element | Ranged ions | Dissociated ions | As-ranged at% | Dissociations added at% | Difference at% |
|---|---|---|---|---|---|
| Li | 433,383 | 0 | 10.01 ± 0.03 | 9.86 ± 0.03 | −0.16 |
| Fe | 847,446 | 0 | 19.58 ± 0.04 | 19.27 ± 0.04 | −0.31 |
| P | 585,562 | 16,564 | 13.53 ± 0.03 | 13.69 ± 0.03 | 0.16 |
| O | 2,461,576 | 52,996 | 56.88 ± 0.05 | 57.18 ± 0.05 | 0.31 |
| Total | 4,327,996 | 69,560 | | | |

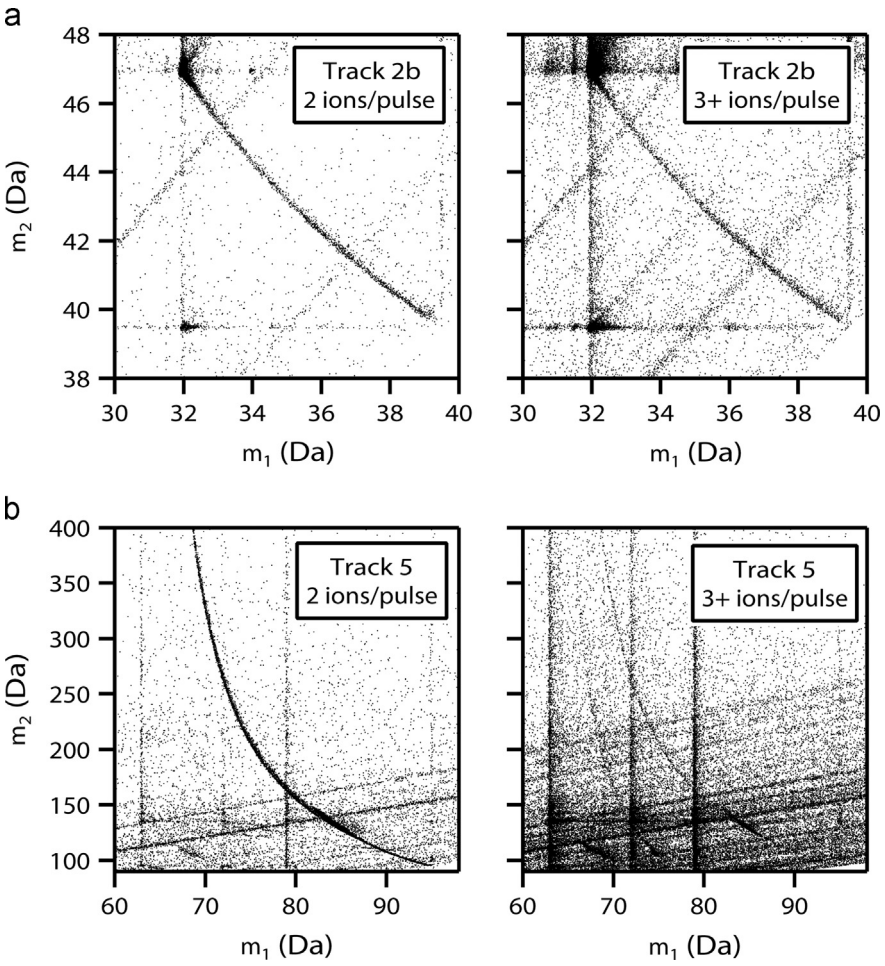


**Fig. 9.** Comparison of dissociation pathways (a) track 2b and (b) track 5 when filtered to ions detected as 2 ions per pulse or 3+ ions per pulse.

composition, increasing the measured oxygen concentration by just 0.3 at%.

## 4. Discussion

Dramatic differences were observed in the measured composition of LFP by green laser and UV laser-assisted field evaporation. Fig. 4 demonstrates that the green laser data exhibits a severe Li deficiency and relatively minor O deficiency while the UV laser data exhibits nominal concentrations of Li but a stronger O deficiency. This artificial Li deficiency is a major concern for the applicability of APT to lithium ion battery materials. Considering the remarkably low evaporation field for Li (14 V/nm) compared to Fe (33 V/nm), the Li deficiency could originate from the selective dc evaporation of Li if the effective pulse fraction is smaller for the green laser than the UV laser. This scenario is potentially consistent with the higher background observed for the green laser mass spectrum in Fig. 2, but comparison of the field evaporation behavior of Si for the green and UV laser systems in Fig. 1 suggests that 200–300 pJ/pulse on the green laser should overlap with the 1–50 pJ/pulse range explored by the UV laser. This comparison assumes, however, that 355 nm and 532 nm wavelengths are absorbed with similar efficiencies, as is the case for Si but appears invalid for $LiFePO_4$. Inspection of the literature reveals that there is a significant difference in the diffuse reflectance, and therefore absorbance, at 355 nm and 532 nm for bulk $LiFePO_4$ [34]. One possible explanation of the unexpected differences in composition as a function of laser wavelength could be that the band gap of $LiFePO_4$ ($\sim$3.9 eV [35]) is comparable to the photon energy of the UV laser (355 nm $\sim$3.5 eV), enabling reliable thermally-assisted field evaporation, but the band gap is substantially greater than the photon energy of the green laser (532 nm $\sim$2.33 eV). This may make it easier for the UV laser to absorb into defect states at the specimen surface than the green laser, but this seems an incomplete explanation since sub-band gap lasers have been used successfully previously for many other oxide materials [16,36–38]. As summarized in review articles by Kelly et al. [39] and Silaeva et al. [40], under the influence of a large electric field, the band gap is depressed for semiconducting and dielectric materials until effectively becoming metallic in nature. The inability of the green laser to achieve a reasonable Li concentration is therefore still perplexing. From an experimental standpoint, if the origin of the Li deficiency for the green laser results from selective dc evaporation loss, exploring higher laser energies with the green laser should improve the overall Li concentration. Although an apparent trend for smaller Li concentrations is apparent when the green laser energy was increased from 200 to 300 pJ/pulse, this represents a very small energy range (factor of 1.5) and a much broader range should be explored to establish more reliable trends (e.g. factor of 50 in the presented UV laser data). Further investigations that also incorporate sophisticated models of surface states and laser-tip interactions could further clarify why $LiFePO_4$ exhibits the strong, wavelength-dependent differences in field evaporation behavior.

APT analyses of many oxides have resulted in non-stoichiometric measurements [14–19], and the origin of these errors is still an active topic of debate. Bachhav et al. [41], after Saxey [31], suggested that quantification of the O loss due to molecular ion dissociation could partially account for the observed O deficiency in Fe-base oxides. This quantification for $LiFePO_4$, shown in Table 2, has a positive but limited effect on the overall composition (improvement by $\sim$0.3 .at% O) due to the small number of counts compared to the overall measurement ($\sim$1.6% of all ranged events). It is therefore unlikely that molecular dissociation, at least by detected tracks, is a dominant O loss mechanism for $LiFePO_4$. Bachhav also suggested that detector pileup effects could be the source of O deficiency. While pileup likely affects the overall composition to some extent, this explanation seems incomplete for $LiFePO_4$ as the percentage of multihits, which is correlated with detector pileup events, is not consistent with the measured trends in O concentration. The distribution of multihit events is plotted for various laser conditions in Fig. 10. Firstly, the green laser data exhibit higher percentages of multihit events than the UV laser data and therefore should exhibit more detector pileup loss, but the green laser data results in a higher O concentration (normalized to Fe+P) than does the UV laser data (see Fig. 4). Secondly, increasing the UV laser energy decreases the percentage of multihits and simultaneously decreases the overall O concentration. Therefore detector pileup seems to be an unlikely source of O deficiency. It is also tempting to identify the 16 Da peak as $^{16}O_2^{2+}$ to improve the overall O concentration [18,42], but recent studies involving loading of Fe- and Si-oxides with $^{18}O$ have conclusively demonstrated that the 16 Da peak should be identified only as $^{16}O^+$ [19,41].

The measured O concentration varied strongly with both laser energy and wavelength. The green laser datasets exhibited remarkably higher concentrations of elemental O and $O_2^+$ species (Fig. 5), which largely accounts for the higher overall O concentration under those analysis conditions. By contrast, the UV laser data contained smaller elemental O peaks and increased concentrations of larger molecular species (e.g. $FePO_3^{2+}$) that were not observed in the green laser mass spectra. Increased concentrations of O were found to be well-correlated with the increased prevalence of $O_2^+$ species for the UV laser data as a function of laser energy. Together this suggests that experimental conditions (laser wavelength and energy) favoring the evaporation of elemental O ionic species is critical to achieving a better overall O stoichiometry.

The observed oxygen loss at higher UV laser energies for LFP is consistent with similar studies on magnesia, ceria and wüstite [16,18,28]. Devaraj et al. and Kirchhofer et al. tentatively explained the increasing O deficiency with laser energy through the formation of neutral oxygen molecules at a lower evaporation fields. They independently argued that decreasing the UV laser energy increases the electric field on the tip (by increasing the standing voltage to maintain the same evaporation rate) which increases the probability of ionization of any desorbed neutral molecules. This hypothesis is, however, unverifiable by APT as the loss of neutral molecules cannot be directly detected. Diercks et al. [33] presented indirect evidence to support this hypothesis in the case of nitride-based materials (neutral $N_2$ sublimation) through interpretation of the background as a function of laser energy and further suggested that this could be a general effect for species that readily form diatomic molecules. However, a debate persists

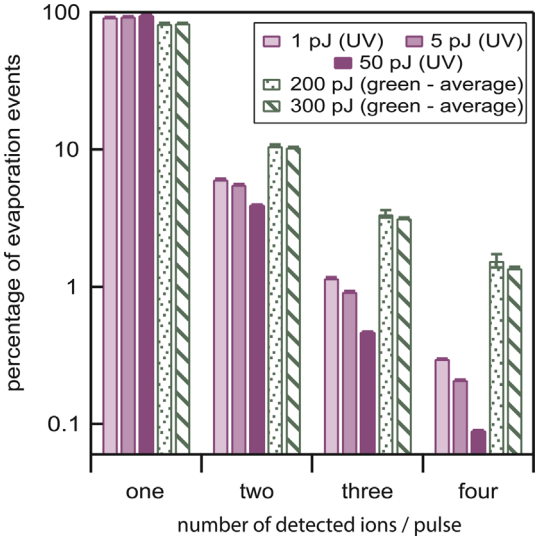


**Fig. 10.** Distribution of number of detected ions/pulse by analysis condition.

within the community about whether or not a neutral molecule could escape the high-field region of the tip without undergoing ionization, similar to that of an imaging gas molecule in field ion microscopy. The ionization of a neutral molecule is undeniably field dependent and probabilistic [26], but further proof is needed through both experiments and modeling to quantify this probability. Nonetheless, our data on $LiFePO_4$ are consistent with these previous observations and the loss of neutral O may partially explain the apparent O deficiency. It is also worth emphasizing again that neutral molecule formation has been clearly identified in the molecular dissociation of $PO_4^+$ (Fig. 6), but this dissociation occurs far from the tip where ionization of the neutral $O_2$ molecule can no longer occur. It is therefore still unclear whether or not neutral $O_2$ could escape the tip without ionization.

Detailed quantification by integration over identified molecular dissociation pathways within the Saxey plots did not significantly affect the overall composition of $LiFePO_4$. However, the exercise of replotting the data as a function of minimum distance versus $\Delta V/V_0$ provided a useful avenue to evaluate the accuracy of the identified pathways and improve our understanding of the mass spectra. For example, the molecular dissociation surrounding track 2b is very well described by the conventional pathway of $^{31}P^{16}O_3^{2+} \rightarrow {}^{31}P^{16}O^+ + {}^{16}O_2^+$, which is made apparent by the minimal variations along the integrated region in Fig. 7. Conversely, replotting the dissociations around track 5 in the same way revealed two distinct regions of the pathway, which was not apparent in the conventional plot of $m_1^{\prime}$ and $m_2^{\prime}$. Intriguingly, the current best-fit for one of these sub-paths suggests that the parent molecule, initially identified as $PO_4^+$, could in fact be the much larger $P_3O_{12}^{3+}$ with the same mass-to-charge-state ratio. Since neither P nor O contain significant concentrations of a second isotope, it is impossible to evaluate fully this possibility, but it suggests that the $PO_x$-type peaks throughout the mass spectra could contain a significant fraction of these larger molecular species. This possibility could partially account for both the observed P and O deficiencies shown in Fig. 4. The analysis of $LiFePO_4$ with a significant fraction of the $^{18}O$ isotope could clarify this question in future experiments. The molecular dissociations around track 5 are also unique in that they appear primarily within two-ion detection events and not higher-order detection events. This suggests that this pathway originates almost exclusively from so-called "golden" events in which a single ion, and only one ion, evaporates and subsequently dissociates into two detected ions. The physical reason behind this observation remains uncertain, but it shows that researchers studying molecular dissociation in APT data should be vigilant of possible differences in behavior between single, double and higher-order detector events.

## 5. Conclusions

The systematic study of laser assisted APT for $LiFePO_4$ provides many insights into the potential and problems associated with APT analyses of lithium ion battery materials with both green and UV laser illumination. Analyses utilizing green laser pulsing yielded substantial Li deficiencies, possibly due to selective dc evaporation of Li from poor absorption of the 532 nm wavelength light inherent to the optical properties of $LiFePO_4$. Conversely, UV laser pulsing provided more accurate Li concentrations but substantial O deficiencies. Decreasing the UV laser energy increases the overall O concentration closer to its nominal value, but does not achieve a stoichiometric composition. Plotting and quantification of the molecular dissociation events could not fully account for the observed O deficiency, but does provide new insights into the field evaporation behavior and suggests that larger $PO_x$ molecular species may evaporate and are not properly accounted for in the current treatment of the mass spectra. These results demonstrate that APT analysis of Li-based battery materials with low-energy UV laser pulsing is generally reliable with some O deficiencies, while green laser pulsing generates unreliable measurements of the Li concentration.

## Acknowledgments

This research is conducted through the support by the Northeastern Center for Chemical Energy Storage, an Energy Frontier Research Center funded by the U.S. Department of Energy (DOE), Office of Basic Energy Sciences (BES), under award number DE-SC0001294, including matching support from NYSTAR-NYSDED. DKS acknowledges separate funding support from DOE-BES in quantifying the molecular dissociation pathways and preparing this manuscript. Fruitful discussions with Dr. Michael Moody, University of Oxford, UK and Dr. Lyle Gordon, Northwestern University and currently Pacific Northwest National Laboratory (PNNL), are acknowledged. We would also like to acknowledge the support of Dr. Michael DiBattista, QCT Failure Analysis Lab, Qualcomm Inc., for providing us with access to several focused ion beam tools for this work. LEAP 4000X HR APT experiments were performed using EMSL, a U.S. DOE Office of Science User Facility sponsored by the Office of Biological and Environmental Research and located at PNNL. PNNL is operated by Battelle for the U.S. DOE under Contract DE-AC05-76RL01830. RLM acknowledges UA' Central Analytical Facility, under the Office for Sponsored Research, and the NSF-MRI-0722631 award for the LEAP 3000X Si APT work conducted.

## References

[1] W.C. Chueh, F. El Gabaly, J.D. Sugar, N.C. Bartelt, A.H. McDaniel, K.R. Fenton, K.R. Zavadil, T. Tyliszczak, W. Lai, K.F. McCarty, Intercalation pathway in many-particle $LiFePO_4$ electrode revealed by nanoscale state-of-charge mapping, Nano Lett. 13 (2013) 866–872.

[2] C. Delmas, M. Maccario, L. Croguennec, F. Le Cras, F. Weill, Lithium deintercalation in LiFePO4 nanoparticles via a domino-cascade model, Nat. Mater. 7 (2008) 665–671.

[3] L. Gu, C. Zhu, H. Li, Y. Yu, C. Li, S. Tsukimoto, J. Maier, Y. Ikuhara, Direct observation of lithium staging in partially delithiated $LiFePO_4$ at atomic resolution, J. Am. Chem. Soc. 133 (2011) 4661–4663.

[4] U. Boesenberg, F. Meirer, Y. Liu, A.K. Shukla, R. Dell'Anna, T. Tyliszczak, G. Chen, J.C. Andrews, T.J. Richardson, R. Kostecki, J. Cabana, Mesoscale phase distribution in single particles of $LiFePO_4$ following lithium deintercalation, Chem. Mater. 25 (2013) 1664–1672.

[5] T.F. Kelly, D.J. Larson, Atom probe tomography 2012, Annu. Rev. Mater. Res 42 (2012) 1–31.

[6] M.P. Moody, B. Gault, L.T. Stephenson, R.K.W. Marceau, R.C. Powles, A.V. Ceguerra, A.J. Breen, S.P. Ringer, Lattice rectification in atom probe tomography: Toward true three-dimensional atomic microscopy, Microsc. Microanal. 17 (2011) 226–239.

[7] B. Gault, M.P. Moody, J.M. Cairney, S.P. Ringer, Atom Probe Microscopy, Springer, New York, NY, 2012.

[8] B.P. Geiser, T.F. Kelly, D.J. Larson, J. Schneir, J.P. Roberts, Spatial distribution maps for atom probe tomography, Microsc. Microanal. 13 (2007) 437–447.

[9] D.E. Perea, E.R. Hemesath, E.J. Schwalbach, J.L. Lensch-Falk, P.W. Voorhees, L.J. Lauhon, Direct measurement of dopant distribution in an individual vapour–liquid–solid nanowire, Nat. Nanotechnol. 4 (2009) 315–319.

[10] A. Biswas, D.J. Siegel, C. Wolverton, D.N. Seidman, Precipitates in Al–Cu alloys revisited: atom-probe tomographic experiments and first-principles calculations of compositional evolution and interfacial segregation, Acta Mater. 59 (2011) 6187–6204.

[11] R. Agrawal, R.A. Bernal, D. Isheim, H.D. Espinosa, Characterizing atomic composition and dopant distribution in wide band gap semiconductor nanowires using laser-assisted atom probe tomography, J. Phys. Chem. C 115 (2011) 17688–17694.

[12] N. Dawahre, G. Shen, S. Balci, W. Baughman, D. Wilbert, N. Harris, L. Butler, R. Martens, S. Kim, P. Kung, Atom probe tomography of zinc oxide nanowires, J. Electron. Mater. 41 (2012) 801–808.

[13] D.J. Larson, R.L. Alvis, D.F. Lawrence, T.J. Prosa, R.M. Ulfig, D.A. Reinhard, P.H. Clifton, S.S.A. Gerstl, J.H. Bunton, D.R. Lenz, T.F. Kelly, K. Stiller, Analysis of bulk dielectrics with atom probe tomography, Microsc. Microanal. 14 (2008) 1254–1255.

[14] K. Hono, T. Ohkubo, Y.M. Chen, M. Kodzuka, K. Oh-ishi, H. Sepehri-Amin, F. Li, T. Kinno, S. Tomiya, Y. Kanitani, Broadening the applications of the atom probe technique by ultraviolet femtosecond laser, Ultramicroscopy 111 (2011) 576–583.
[15] E.A. Marquis, N.A. Yahya, D.J. Larson, M.K. Miller, R.I. Todd, Probing the improbable: imaging C atoms in alumina, Mater. Today 13 (2010) 34–36.
[16] A. Devaraj, R. Colby, W.P. Hess, D.E. Perea, S. Thevuthasan, Role of photo-excitation and field ionization in the measurement of accurate oxide stoichiometry by laser-assisted atom probe tomography, J. Phys. Chem. Lett. 4 (2013) 993–998.
[17] C.A. Williams, G.D.W. Smith, E.A. Marquis, Quantifying the composition of yttrium and oxygen rich nanoparticles in oxide dispersion strengthened steels, Ultramicroscopy 125 (2013) 10–17.
[18] M. Bachhav, R. Danoix, F. Danoix, B. Hannoyer, S. Ogale, F. Vurpillot, Investigation of wustite ($Fe_{1-x}O$) by femtosecond laser assisted atom probe tomography, Ultramicroscopy 111 (2011) 584–588.
[19] T. Kinno, M. Tomita, T. Ohkubo, S. Takeno, K. Hono, Laser-assisted atom probe tomography of $^{18}O$-enriched oxide thin film for quantitative analysis of oxygen, Appl. Surf. Sci. 290 (2014) 194–198.
[20] K. Thompson, D. Lawrence, D.J. Larson, J.D. Olson, T.F. Kelly, B. Gorman, In situ site-specific specimen preparation for atom probe tomography, Ultramicroscopy 107 (2007) 131–139.
[21] Y. Janssen, D. Santhanagopalan, D. Qian, M. Chi, X. Wang, C. Hoffmann, Y.S. Meng, P.G. Khalifah, Reciprocal salt flux growth of $LiFePO_4$ single crystals with controlled defect concentrations, Chem. Mater. 25 (2013) 4574–4584.
[22] D.R. Kingham, The post-ionization of field evaporated ions: a theoretical explanation of multiple charge states, Surf. Sci. 116 (1982) 273–301.
[23] R. Haydock, D.R. Kingham, Post-ionization of field-evaporated ions, Phys. Rev. Lett. 44 (1980) 1520–1523.
[24] Y. Amouyal, D.N. Seidman, Atom probe tomography of nickel-based superalloys with green or ultraviolet lasers: a comparative study, Microsc. Microanal. 18 (2012) 971–981.
[25] M.D. Mulholland, D.N. Seidman, Voltage-pulsed and laser-pulsed atom probe tomography of a multiphase high-strength low-carbon steel, Microsc. Microanal. 17 (2011) 950–962.
[26] M.K. Miller, A. Cerezo, M.G. Hetherington, G.D.W. Smith, Atom probe field ion microscopy, Oxford University Press, USA, 1996.
[27] L.M. Gordon, L. Tran, D. Joester, Atom probe tomography of apatites and bone-type mineralized tissues, ACS Nano 6 (2012) 10667–10675.
[28] R. Kirchhofer, M.C. Teague, B.P. Gorman, Thermal effects on mass and spatial resolution during laser pulse atom probe tomography of cerium oxide, J. Nucl. Mater. 436 (2013) 23–28.
[29] J.H. Bunton, J.D. Olson, D.R. Lenz, T.E. Kelly, Advances in pulsed-laser atom probe: Instrument and specimen design for optimum performance, Microsc. Microanal. 13 (2007) 418–427.
[30] G.-H. Greiwe, Z. Balogh, G. Schmitz, Atom probe tomography of lithium-doped network glasses, Ultramicroscopy 141 (2014) 51–55.
[31] D.W. Saxey, Correlated ion analysis and the interpretation of atom probe mass spectra, Ultramicroscopy 111 (2011) 473–479.
[32] T.T. TSong, Y. Liou, Time-of-flight energy and mass analysis of metal-halide ions and their formation and dissociation, Phys. Rev. Lett. 55 (1985) 2180–2183.
[33] D.R. Diercks, B.P. Gorman, R. Kirchhofer, N. Sanford, K. Bertness, M. Brubaker, Atom probe tomography evaporation behavior of *C*-axis GaN nanowires: crystallographic, stoichiometric, and detection efficiency aspects, J. Appl. Phys. 114 (2013) 184903.
[34] K. Zaghib, A. Mauger, J.B. Goodenough, F. Gendron, C.M. Julien, Electronic, optical, and magnetic properties of $LiFePO_4$: small magnetic polaron effects, Chem. Mater. 19 (2007) 3740–3747.
[35] F. Zhou, K. Kang, T. Maxisch, G. Ceder, D. Morgan, The electronic structure and band gap of $LiFePO_4$ and $LiMnPO_4$, Solid State Commun. 132 (2004) 181–186.
[36] Y.M. Chen, T. Ohkubo, K. Hono, Laser assisted field evaporation of oxides in atom probe analysis, Ultramicroscopy 111 (2011) 562–566.
[37] B. Mazumder, A. Vella, B. Deconihout, T.a. Al-Kassab, Evaporation mechanisms of MgO in laser assisted atom probe tomography, Ultramicroscopy 111 (2011) 571–575.
[38] S. Gin, J.V. Ryan, D.K. Schreiber, J. Neeway, M. Cabie, Contribution of atom-probe tomography to a better understanding of glass alteration mechanisms: application to a nuclear glass specimen altered 25 years in a granitic environment, Chem. Geol. 349 (2013) 99–109.
[39] T.F. Kelly, A. Vella, J.H. Bunton, J. Houard, E.P. Silaeva, J. Bogdanowicz, W. Vandervorst, Laser pulsing of field evaporation in atom probe tomography, Curr. Opin. Solid State Mater. Sci. 18 (2014) 81–89.
[40] E.P. Silaeva, M. Karahka, H.J. Kreuzer, Atom probe tomography and field evaporation of insulators and semiconductors: theoretical issues, Curr. Opin. Solid State Mater. Sci. 17 (2013) 211–216.
[41] M. Bachhav, F. Danoix, B. Hannoyer, J.M. Bassat, R. Danoix, Investigation of O-18 enriched hematite (alpha-$Fe_2O_3$) by laser assisted atom probe tomography, Int. J. Mass Spectrom. 335 (2013) 57–60.
[42] E. Talbot, R. Larde, P. Pareige, L. Khomenkova, K. Hijazi, F. Gourbilleau, Nanoscale evidence of erbium clustering in Er-doped silicon-rich silica, Nanoscale Res. Lett. 8 (2013) 39.